Supplementary Information

Photothermally induced natural vibration for versatile and high-speed actuation of crystals

Yuki Hagiwara[1], Shodai Hasebe[1], Hiroki Fujisawa[2], Junko Morikawa[2], Toru Asahi[1,3], Hideko Koshima[3*]

[1] Graduate School of Advanced Science and Engineering, Waseda University, 3-4-1 Okubo, Shinjuku-ku, Tokyo 169–8555, Japan.

[2] School of Materials and Chemical Technology, Tokyo Institute of Technology, 2-12-1 Ookayama, Meguro-ku, Tokyo 152-8550, Japan.

[3] Research Organization for Nano & Life Innovation, Waseda University, 513 Wasedatsurumaki-cho, Shinjuku-ku, Tokyo 162-0041, Japan.

[*]Correspondence to Email: h.koshima@kurenai.waseda.jp

Contents

1. Crystal structure

Supplementary Table 1 Crystal structure of the **1β** crystal at 20 °C

Temperature (°C)	20
Formula	$C_7H_6N_2O_5$
Formula Weight	198.14
Crystal System	Monoclinic
Space Group	$P2_1/n$
a (Å)	3.9723(9)
b (Å)	13.700(3)
c (Å)	15.431(4)
α (°)	90
β (°)	91.128(6)
γ (°)	90
Z	4
V (Å^3)	839.6(3)
d_{calc} (g cm^{-3})	1.567
R_1 [$I > 2\sigma$(I)]	0.0604
wR_2 [$I > 2\sigma$(I)]	0.1400
GOF	1.038

2. Measurements of thermal properties

a

Temp. (°C)	*a* (Å)	*b* (Å)	*c* (Å)	*α* (°)	*β* (°)	*γ* (°)	*V* (Å^3)
10	3.972(3)	13.742(12)	15.465(6)	90.05(9)	91.06(4)	90.02(4)	844(2)
20	3.984(7)	13.733(25)	15.489(16)	90.06(8)	91.01(4)	90.11(7)	847(2)
30	3.993(4)	13.753(9)	15.489(34)	90.10(7)	90.84(3)	90.09(4)	850(1)
40	4.002(7)	13.754(8)	15.477(27)	90.04(4)	90.83(5)	89.92(18)	851(1)
50	4.015(5)	13.757(9)	15.451(12)	89.98(12)	90.89(2)	90.00(4)	853(1)
60	4.021(3)	13.762(19)	15.457(22)	90.01(2)	90.76(5)	90.08(3)	855(2)

( ): Standard deviation, $n = 3$

b

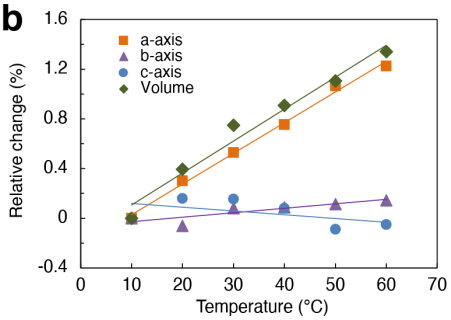

c

	Thermal expansion coefficient (MK^{-1})
a-axis	247
b-axis	36.0
c-axis	-30.5
Volume	257

d

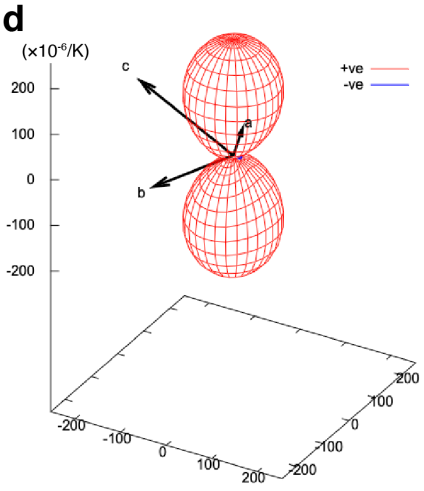

Supplementary Fig. 1 Thermal expansion of **1β** crystal. **a** Summary of temperature dependence of lattice constants. **b** Relative changes of three axes lengths and the volume by temperature change. **c** Summary table of thermal expansion coefficients. **d** Thermal expansivity indicatrix calculated using PASCal.[S1]

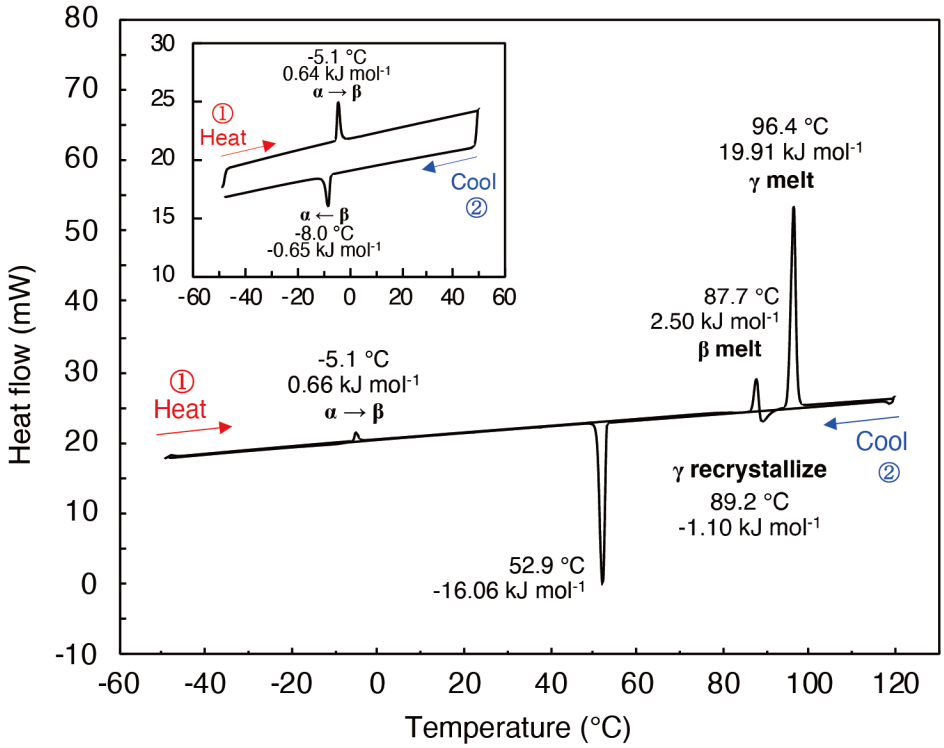

Supplementary Fig. 2 Differential scanning calorimetry curve of crystals of **1** at a speed of 10 °C min^{-1} on heating and subsequent cooling.

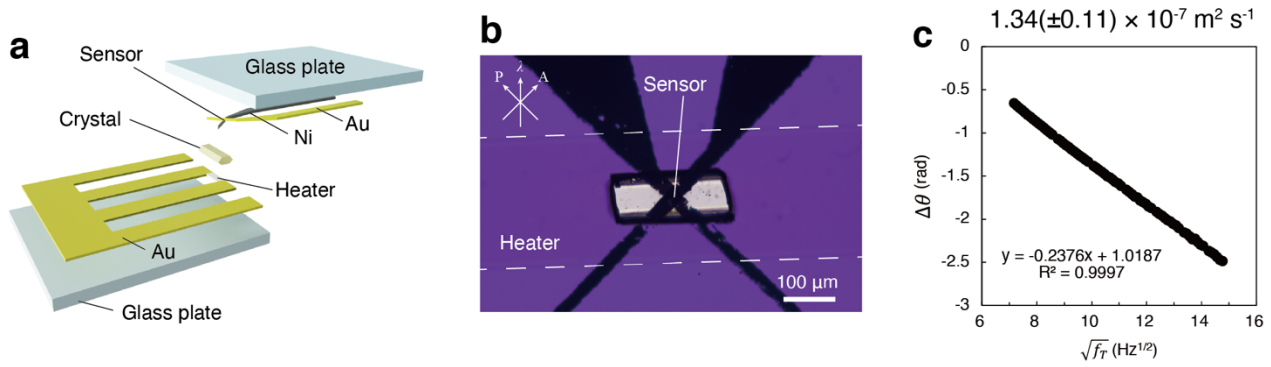

Supplementary Fig. 3 Thermal diffusivity measurement of a **1β** crystal by temperature wave analysis (TWA). [S2–5] **a** Schematic assembly of samples for TWA measurement. **b** Polarized photo of a **1β** crystal (thickness: 49.2 μm) between the heater and the sensor. **c** The plot of phase delay $\Delta\theta$ and square root of temperature wave frequency f_T in the range from 51.3 to 251.5 Hz (kd = 1.71–3.94).

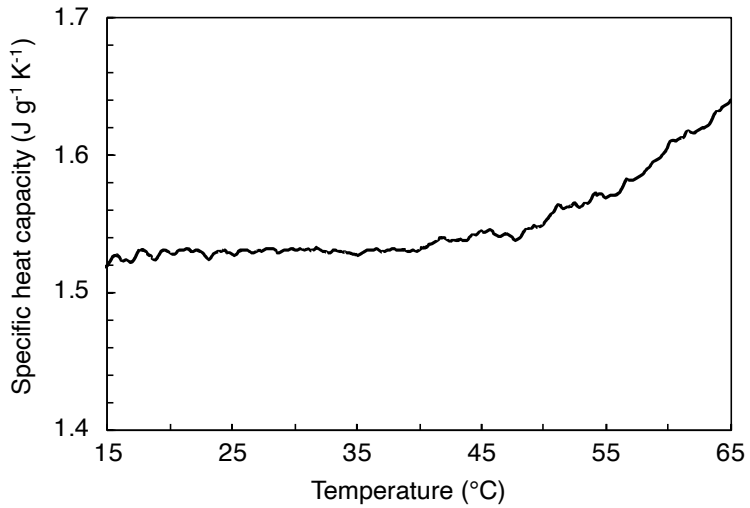

Supplementary Fig. 4 Temperature dependence of heat capacity of **1β** crystals.

3. Fluorescence spectrum measurement

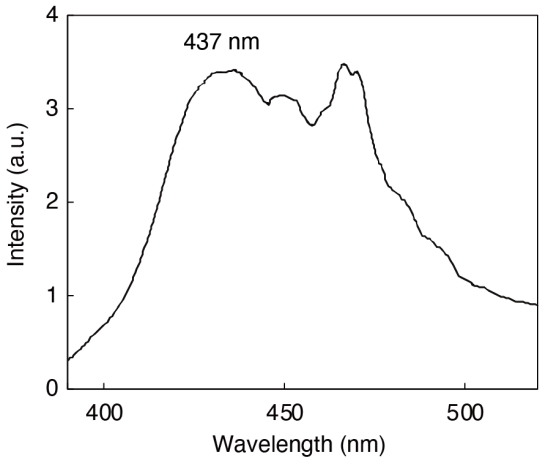

Supplementary Fig. 5 Fluorescence spectrum (λ_{ex} = 300 nm) of powdered **1β** crystals with a peak at 437 nm. Peaks around 450–480 nm are derived from the apparatus.

The fluorescence quantum yield (λ_{ex} = 375 nm) of the **1β** single crystals was determined to be 0.005 with an absolute photoluminescence quantum yield spectrometer.

4. Young's modulus measurement

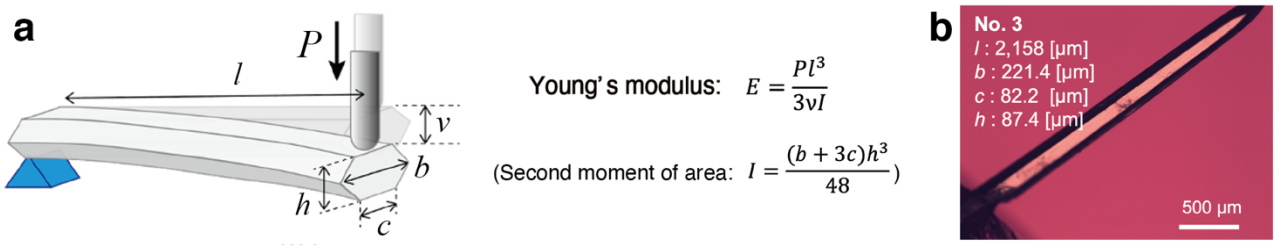

c

Sample No.	n	Length l (μm)	Width b (μm)	Top width c (μm)	Thickness h (μm)	Young's modulus E (GPa)	
						Mean	SE
1	6	3,497	258.8	134.9	193.2	1.68	0.06
2	5	2,650	177.3	67.2	130.2	1.69	0.10
3	6	2,158	221.4	82.2	87.4	1.71	0.14
4	6	1,835	181.1	57.2	83.7	1.48	0.04
5	4	2,130	126.4	31.0	90.7	1.71	0.10

Supplementary Fig. 6 Young's modulus measurement of **1β** crystals by cantilever bending test. **a** Illustration of the crystal cantilever with an applied force *P*. **b** Polarized photo of a measured crystal viewed from the top (sample No.5). **c** Summary table of the measured Young's modulus of crystals with various shapes.

Young's modulus of the **1β** crystal was measured using a force load machine (RTG-1210, A&D). The tip of a single crystal was fixed to a glass plate as a support, and the other tip was free to move vertically. The free tip was pressed in the vertical downward direction by the jig at the rate of 200 μm min^{-1}, and the jig displacement dependence of the load force was measured during the compression of the free tip. Such bending test used five crystals of **1β** and repeated several times for each crystal, and the Young's modulus was estimated to be **1.65 (0.04) GPa**.

5. Natural vibration induced by the photothermal effect

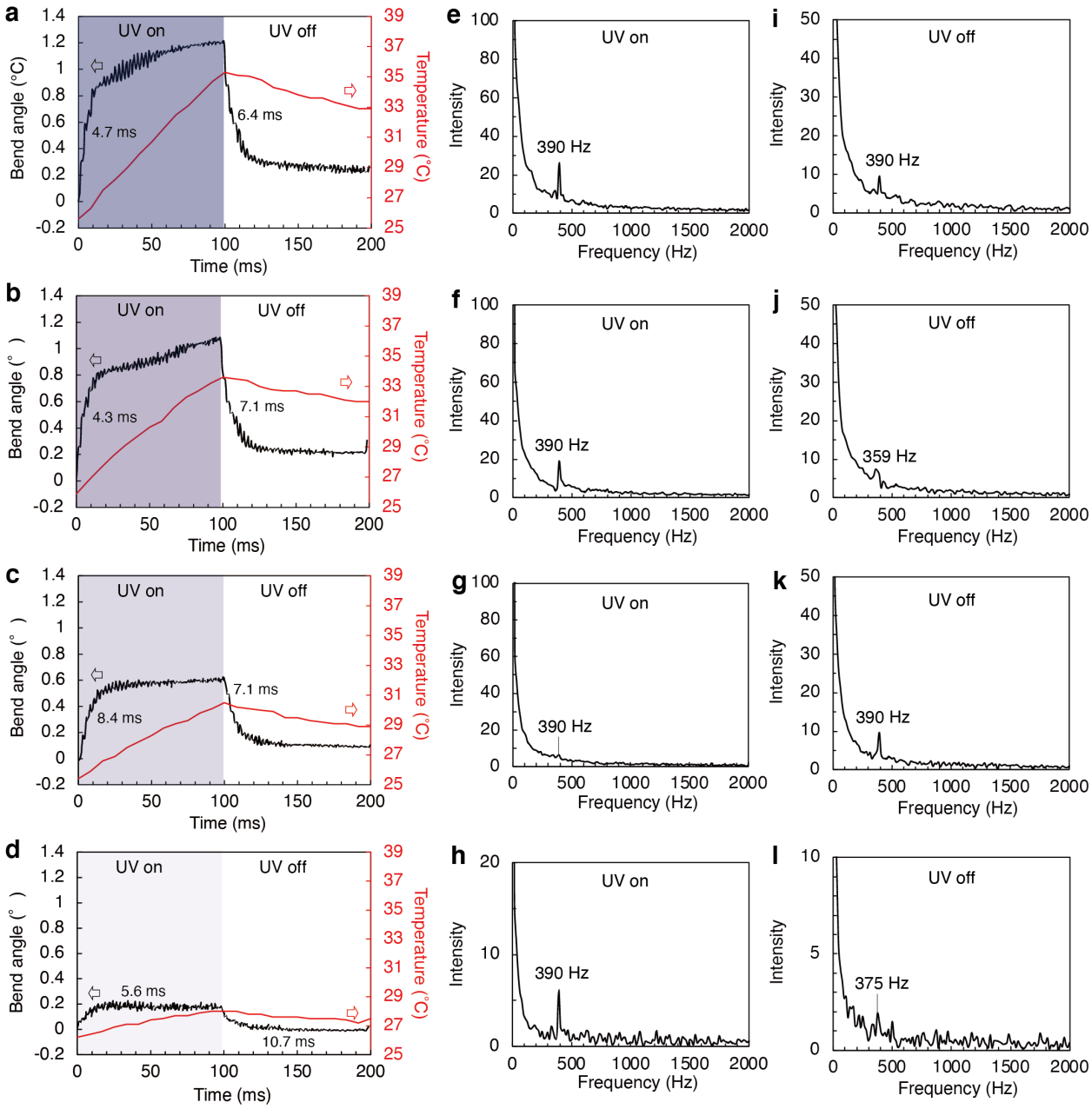

m

UV intensity (mW cm^{-2})	Large photothermal bending		Natural vibration			
			UV on		UV off	
	Maximum bend angle (°)	maximum temperature (°C)	Maximum bend angle (°)	Natural frequency (Hz)	Maximum bend angle (°)	Natural frequency (Hz)
1456	1.218	35.3	0.198	390	0.173	390
1219	1.085	33.6	0.152	390	0.119	359
642	0.624	30.5	0.101	390	0.0770	390
160	0.226	27.5	0.0595	390	0.0410	375

Supplementary Fig. 7 a–d Time profiles of crystal III bending (black line) and top surface temperature (red line) upon UV irradiation at (**a**) 1456, (**b**) 1219, (**c**) 642, (**d**) 160 mW cm^{-2} for 100 ms and after the UV cessation. The numbers in the graphs indicate time constants. **e–l** Fourier transform analyses with and without UV irradiation at (**e, i**) 1456, (**f, j**) 1219, (**g, k**) 642, (**h, l**) 160 mW cm^{-2} for 100 ms. **m** Summary table of the photothermally driven bending with the natural vibration at various UV intensities.

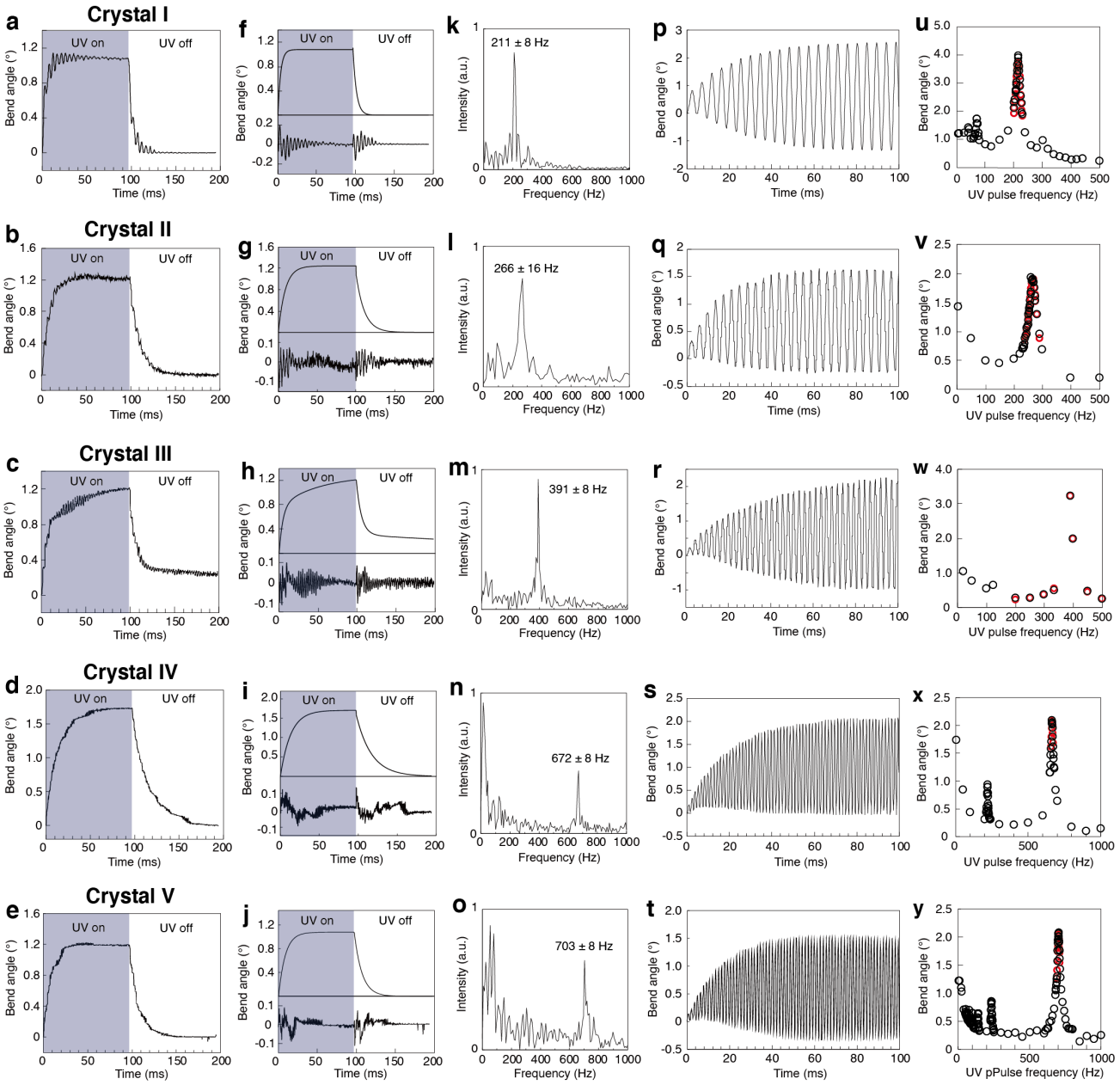

Supplementary Fig. 8 Photothermally driven bending of various shape crystals I–V with natural vibrations of **I.** 216, **II**. 268, **III**. 390, **IV.** 664, **V.** 702 Hz. The detail shape information is shown in Supplementary Table 2. (**a–e**) Time dependence of the bend angle under and after irradiation of UV for 100 ms. (**f–j**) Time profile of the fitted exponential curve of the large photothermally driven bending (upper) and the extracted natural vibration (lower) of **a–e**. (**k–o**) Graphs of Fourier transform analyses of **a–e**. (**p–t**) Time dependence of the resonated bending of the natural vibration under pulsed UV irradiation of the natural frequency. (**u–y**) Relationship between pulse frequency and maximum bend angle: experimental (black) and fitted (red) bend angles (see the footnote in Supplementary Table 2).

Supplementary Table 2 Summary of crystal shape, photothermally driven bending, non-resonated natural vibration, and resonated natural vibration of crystals I–V.

	I	II	III	IV	V
Crystal shape					
Length l /μm	5,100	8,419	6,075	8,180	5,444
Width b /μm	163	178	151	295	298
Top width c /μm	47	116	40	127	173
Thickness h /μm	48	124	105	215	136
Weight m /μg	40.3	240	95.5	581	273
Photothermally driven bending					
Bend angle under UV for 100ms /°	1.145	1.298	1.216	1.741	1.224
Time constants τ_{on} /ms	3.5	8.7	4.7	13.2	8.5
Time constants τ_{off} /ms	4.1	10.7	6.4	19.4	9.9
Tip speed v_l /m s^{-1}	0.029	0.022	0.013	0.019	0.014
Energy conversion efficiency η	1.56×10^{-7}	4.79×10^{-7}	1.14×10^{-7}	1.28×10^{-6}	3.90×10^{-7}
Non-resonated natural vibration					
Measured natural frequency f /Hz	216	266	390	664	702
Fitted natural frequency f_{fit} /Hz **a)**	216	268	390	666	702
Calculated natural frequency f_{cal} /Hz	262	274	397	476	707
Bend angle under UV for 100ms /°	0.316	0.201	0.198	0.094	0.065
Tip speed v_l /m s^{-1}	0.019	0.025	0.026	0.028	0.014
Energy conversion efficiency η	6.73×10^{-8}	6.16×10^{-7}	4.66×10^{-7}	2.85×10^{-6}	3.86×10^{-7}
Resonated natural vibration					
Bend angle under UV pulse of f Hz /°	3.984	1.851	3.381	2.054	2.082
Resonance amplification ratio	12.6	9.21	17.1	21.9	32
Tip speed v_l /m s^{-1}	0.24	0.23	0.41	0.62	0.44
Energy conversion efficiency η	1.05×10^{-5}	5.22×10^{-5}	1.19×10^{-4}	1.37×10^{-3}	4.05×10^{-4}

a) To calculate the fitted natural frequency f_{fit}, the relationship between UV pulse frequency and the measured maximum bend angle (Supplementary Fig. 5u–y) was fitted to the model of the forced vibration with the damping, as shown in the equation below:

$$\theta(f_p) = \frac{\theta_{st}}{\sqrt{\left\{1 - \left(\frac{f_p}{f_{fit}}\right)^2\right\}^2 + \left\{2\zeta\left(\frac{f_p}{f_{fit}}\right)^2\right\}^2}}$$

where f_p is the UV pulse frequency, $\theta(f_p)$ is the maximum bend angle at the certain pulse frequency, and θ_{st} and ζ are fitting parameters: the static deflection angle and the damping ratio, respectively. As a result, the fitted natural frequency is firmly coincident with the measured natural frequency.

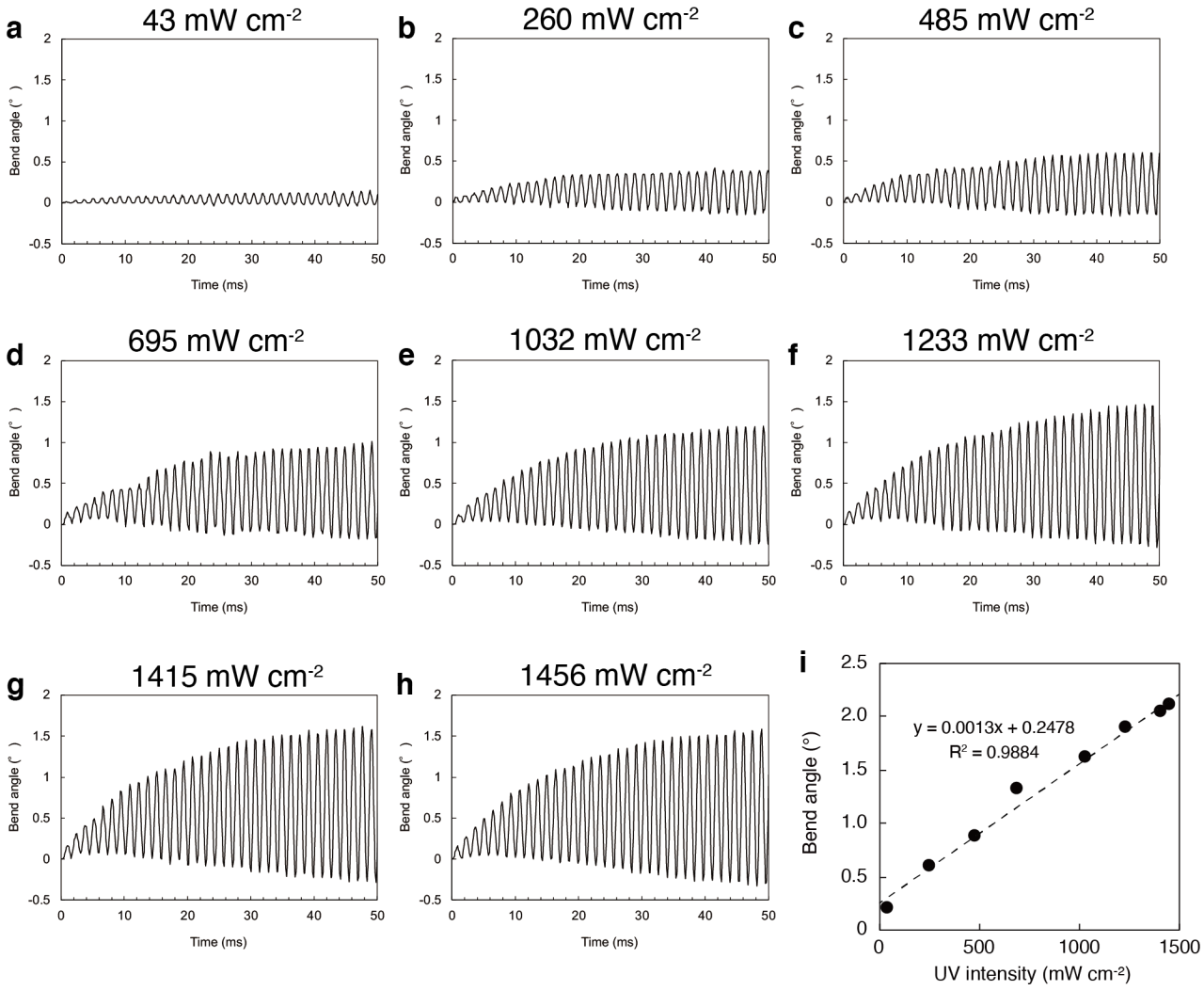

Supplementary Fig. 9 a–h Time profiles of resonated natural vibration of crystal V upon 702 Hz pulsed UV irradiation at (**a**) 43, (**b**) 260, (**c**) 485, (**d**) 695, (**e**) 1032, (**f**) 1233, (**g**) 1415, (**h**) 1456 mW cm^{-2}. **i** UV light intensity dependence of the maximum bend angle upon 702 Hz pulse UV irradiation.

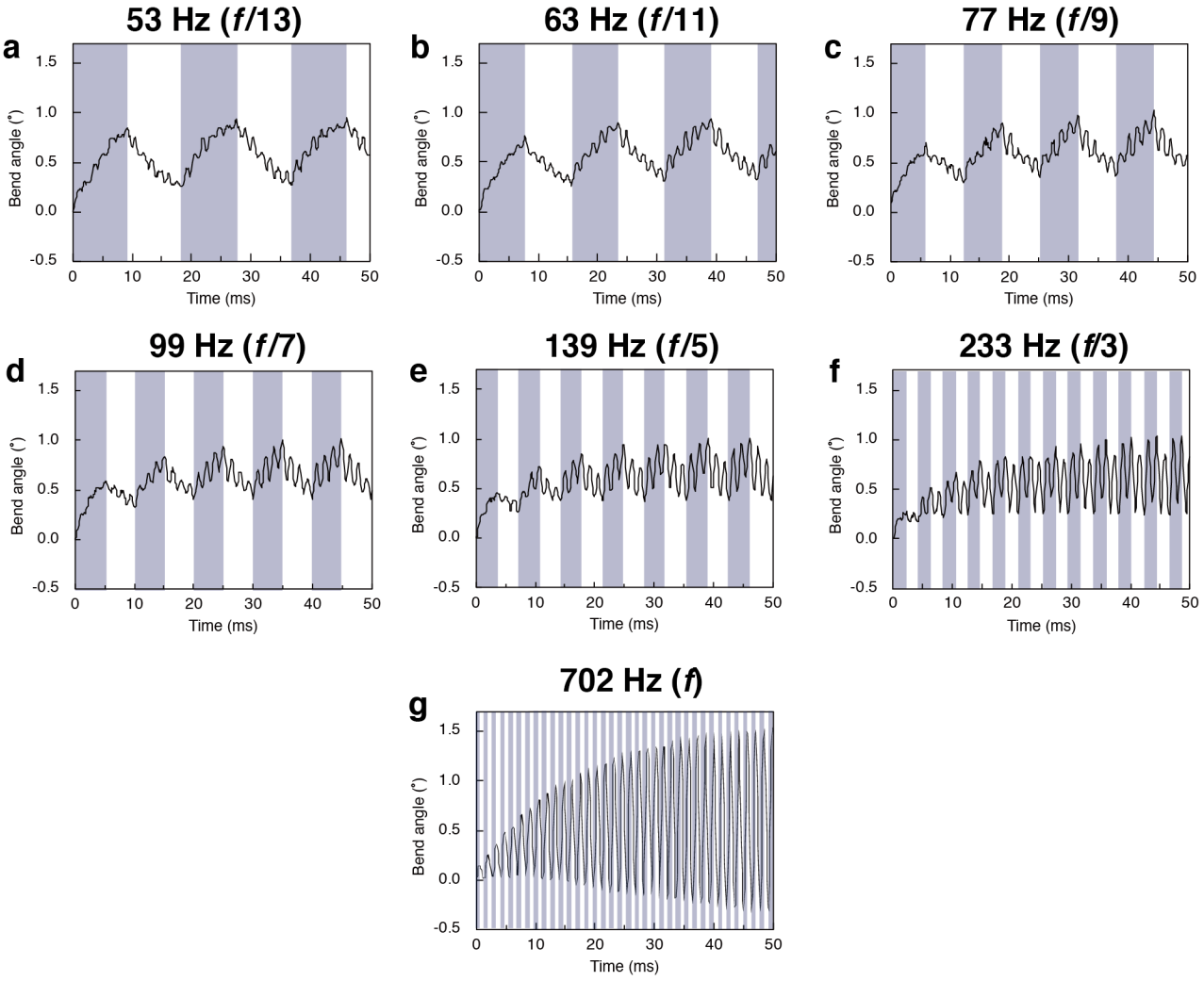

Supplementary Fig. 10 Time profiles of high-speed bending of crystal V upon UV pulse irradiation of (**a**) 53, (**b**) 63, (**c**) 77, (**d**) 99, (**e**) 139, (**f**) 233 Hz, (**g**) 702 Hz.

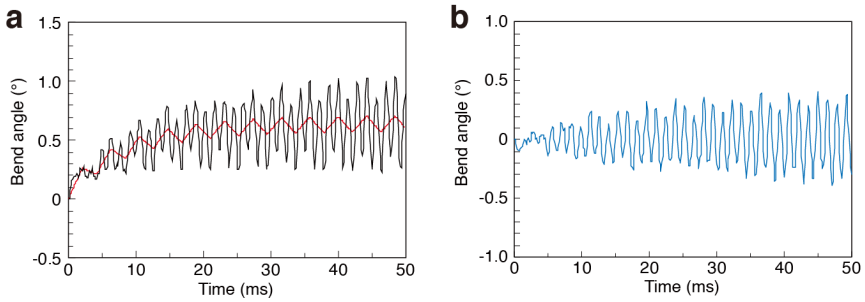

Supplementary Fig. 11 Evaluation method of magnification of the natural vibration during high-speed bending of odd fractions of the natural frequency (e. g. 233 Hz of crystal V). **a** Experimental high-speed bending (black) and the fitted photothermally driven bending (red) under pulsed UV irradiation. **b** Time profile of the extracted natural vibration.

Based on the results of the exponential fitting of the bending profile when irradiated with UV light for 100 ms, we constructed a fitting system for producing the fitted photothermal bending under any frequency UV pulse. According to the fitted bend angle under UV irradiation for 100 ms, the maximum bending angle A and time constants τ_{on} and τ_{off} were provided as constants. The bend angle θ_{on} (t_{on}) under UV irradiation and the bend angle θ_{off} (t_{off}) after UV irradiation were represented, as shown in equations (5.1) and (5.2), respectively:

$$\theta_{on}(t_{on}) = A\left(1 - \exp\left(-\frac{t}{\tau_{on}}\right)\right) \tag{5.1}$$

$$\theta_{off}(t_{off}) = A\exp\left(-\frac{t}{\tau_{off}}\right) \tag{5.2}$$

For reproducing the photothermal bending under UV pulse irradiation, the time t_{on} and t_{off} was corrected to substitute corrected times to equations (5.1) and (5.2) every time UV on/off is switched, using equations (5.3) and (5.4):

$$t_{on} = -\tau_{on}\ln\left(1 - \frac{\theta_{on}(t_{on})}{A}\right) \tag{5.3}$$

$$t_{off} = -\tau_{off}\ln\frac{T - T_0}{A} \tag{5.4}$$

As a result, the fitted photothermal bending was reproduced to behave periodically accompanying with the gradual bend angle increase, as shown in red curve in Supplementary Fig.11a. The bend angle of natural vibration was extracted by subtracting the bend angle of the fitted photothermal bending from the experimental bend angle (black, Supplementary Fig. 11a), as shown in Supplementary Fig. 11b.

Supplementary Table 3 Summary of the tip deflection speed, energy conversion efficiency and crystal shape of **1β** and other previously reported crystals.[S5–7]

Crystal		Tip speed /m s^{-1}	Energy conversion efficiency	Shape		
				Length /μm	Width /μm	Thickness / μm
Resonated natural vibration						
1β	I	0.24	1.05×10^{-5}	5,100	163	48
	II	0.23	5.22×10^{-5}	8,419	178	124
	III	0.41	1.19×10^{-4}	6,075	151	105
	IV	0.62	1.37×10^{-3}	8,180	295	215
	V	0.44	4.05×10^{-4}	5,444	298	136
Non-resonated natural vibration						
1β	I	0.019	6.73×10^{-8}	5,100	163	48
	II	0.025	6.16×10^{-7}	8,419	178	124
	III	0.026	4.66×10^{-7}	6,075	151	105
	IV	0.028	2.85×10^{-6}	8,180	295	215
	V	0.014	3.86×10^{-7}	5,444	298	136
Photothermally driven bending						
1β	I	0.029	1.57×10^{-7}	5,100	163	48
	II	0.022	4.79×10^{-7}	8,419	178	124
	III	0.013	1.14×10^{-7}	6,075	151	105
	IV	0.019	1.28×10^{-6}	8,180	295	215
	V	0.014	3.90×10^{-7}	5,444	298	136
2		0.013	1.05×10^{-7}	1,912	48.2	35.4
3β		0.046	1.04×10^{-6}	5,600	65	34
4		0.003	4.98×10^{-7}	2,910	331	194
5		0.001	1.85×10^{-7}	2,030	344	174
Photoisomerization						
2		6.4×10^{-4}	1.72×10^{-12}	1,170	14.5	10.2
3α		1.4×10^{-4}	7.24×10^{-16}	167	15	0.5
4		8.9×10^{-4}	5.90×10^{-11}	385	30	3.8
5		2.5×10^{-4}	4.19×10^{-12}	171	17.2	2.4

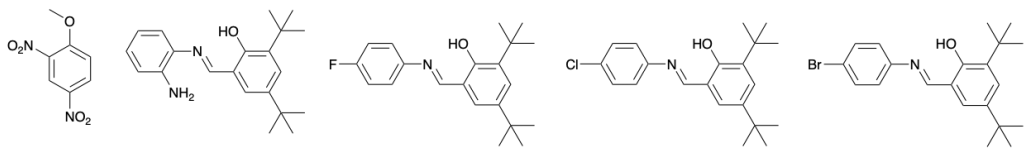

1 **2** [S5] **3** [S6] **4** [S7] **5** [S7]

6. Simulation of crystal bending

The finite element analysis (FEA) is a method of discretizing an object by dividing it into multiple meshes, creating equations of balance for each mesh, and then solving the equations for the entire structure assembled from these meshes. In this research, the bending simulation is performed based on FEA using ANSYS analysis software.[S8]

Ⅰ. Preparation of the crystal cantilever sample

To conduct FEA, physical properties of **1β** crystals and the three-dimensional geometry are required. The thermal diffusivity is applied for the non-steady heat conduction analysis, and density, thermal expansion coefficient, and Young's modulus are applied for the coupled thermo-structural analysis. The three-dimensional geometry of the hexagonal cantilever is prepared by the computer aided design software SpaceClaim.[S8]

Ⅱ. Temperature gradient estimation by the non-steady heat conduction analysis

To perform the non-steady heat conduction analysis, suitable meshing is required for heat conduction along the thickness direction. In this research, the cross-section surface was equally meshed into 4 μm square (Supplementary Fig. 12a). The initial temperature T_0 was set to be the temperature of the crystal area in an IR thermography before UV laser irradiation, 25.6 °C. The atmospheric temperature was set to be the constant temperature of the atmospheric area, 25.2 °C. For temperature gradient estimation, the fitted temperatures obtained by results of thermography were used to adopt temperatures of the top and two upper slanting surfaces.

Ⅲ. Bend angle calculation by the coupled thermo-structural analysis

The crystal cantilever deformation is calculated by the coupled thermo-structural analysis, the time history response analysis using thermal load as an external force estimated from the result of the previous non-steady heat conduction analysis. This analysis evaluates time dependence of shape deformation of the meshed crystal cantilever. Meshing and boundary condition are described as Supplementary Fig. 12b. At first, the long direction of the crystal cantilever was equally meshed by 50 μm per mesh. The cross-section surface was also meshed to several meshes to reflect the temperature gradient along the thickness direction. Then, one tip of the cross-section surface is set to be the fixed tip, and the result of the non-steady heat conduction analysis is applied as the ramped thermal load. The gravitational acceleration was applied in the vertical downward direction for the precise consideration of the tip displacement. The damping ratio ζ is set as an attenuation factor in reference to the equation (6.1):

$$\zeta = \frac{\gamma}{4\pi f} \tag{6.1}$$

where γ is the Rayleigh damping (fitting parameter), and f is the natural frequency.

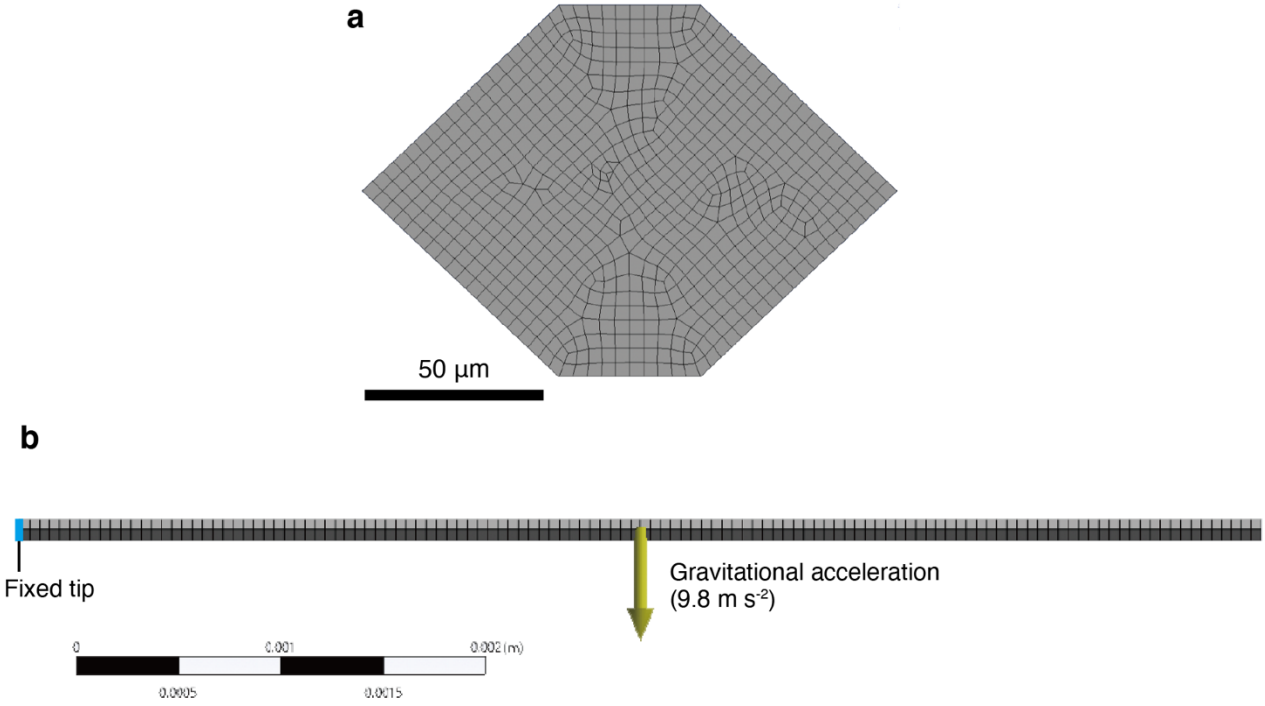

Supplementary Fig. 12 Meshing and boundary condition for FEA. **a** Meshing of the cross-section surface for the non-steady heat conduction analysis. **b** Meshing along the length direction and boundary conditions for the coupled thermo-structural analysis.

6.1. Simulation I of bending of crystal III based on surface temperature measurement

For the simulation I, three types of input temperatures were determined from the measured temperature distribution by an IR thermography camera for setting to three sections of the top and two upper slanting surfaces (A, B, and C) (Supplementary Fig. 13a). First, the temperature distribution along the width direction was considered from results of the IR thermography (Supplementary Fig. 13b). The position dependence of the temperature was extracted on the measured line (10 points) upon UV irradiation for 100 ms (Supplementary Fig. 13c) and fitted as the trapezoid (two linear regression lines and three constant lines), resulting in determination of the crystal position and the temperature set points of the areas A, B, and C (T_A, T_B, and T_C, respectively) (Supplementary Fig. 13d). Thus, T_A is set to the same temperature as the top surface temperature due to the trapezoid approximation. However, T_B and T_C are not placed on the measurement points I–VI and could not directly adopt the temperatures at measured points. For determining T_B and T_C, time dependence of temperatures at the six points I–VI (Supplementary Fig. 13e) were fitted to exponential curves for extracting position dependence of the fitted values of A, $\tau_{UV\,on}$, and $\tau_{UV\,off}$, in accordance with the fitted single-exponential equations (6.2) and (6.3), the temperature change upon UV irradiation ($T_{UV\,on}$) and after the cessation of UV light ($T_{UV\,off}$), respectively:

$$T_{UV\,on}(t) = A\left(1 - \exp\left(-\frac{t}{\tau_{UV\,on}}\right)\right) + T_0 \tag{6.2}$$

$$T_{UV\,off}(t) = (T_{max} - T_0)\exp\left(-\frac{t}{\tau_{UV\,off}}\right) + T_0 \tag{6.3}$$

where t is the time, $T_{UV\,on}(t)$ is the temperature upon UV irradiation at a certain t, A is the constant value, $\tau_{UV\,on}$ is the time constant of the temperature increase upon UV irradiation, and T_0 is the initial temperature of the crystal (25.6 °C), $T_{UV\,off}(t)$ is the temperature after removing UV irradiation at a certain t, T_{max} is the temperature upon UV irradiation for 100 ms, coincident with the maximum temperature of each point in Supplementary Fig. 13d, $\tau_{UV\,off}$ is the time constant of the temperature decrease after removing UV irradiation. Supplementary Fig. 13f, g show the position dependence of the fitted values A and $\tau_{UV\,on}$, respectively, and both graphs were fitted to quadratic equations (inset functions in Supplementary Fig. 13f, g) at high R^2 values. As a result, temperatures of areas B and C upon UV irradiation ($T_{B,\,UV\,on}$ and $T_{C,\,UV\,on}$, respectively) are described as equations (6.4) and (6.5), respectively:

$$T_{B,UV\,on}(t) = 26.1\left(1 - \exp\left(-\frac{t}{239\ \mathrm{ms}}\right)\right) + 25.6\ [°\mathrm{C}] \tag{6.4}$$

$$T_{C,UV\,on}(t) = 17.5\left(1 - \exp\left(-\frac{t}{181\ \mathrm{ms}}\right)\right) + 25.6\ [°\mathrm{C}] \tag{6.5}$$

Supplementary Fig. 13h indicates the relationship between T_{max}-T_0 and $\tau_{UV\,off}$ and was highly fitted to linear regression (inset function). As a result, temperatures of areas B and C after stopping UV irradiation ($T_{B,\,UV\,off}$ and $T_{C,\,UV\,off}$, respectively) are described as equations (6.6) and (6.7), respectively:

$$T_{B,UV\,off}(t) = 8.93\exp\left(-\frac{t}{373\ \mathrm{ms}}\right) + 25.6\ [°\mathrm{C}] \tag{6.6}$$

$$T_{C,UV\,off}(t) = 7.44\exp\left(-\frac{t}{315\ \mathrm{ms}}\right) + 25.6\ [°\mathrm{C}] \tag{6.7}$$

In summary, the time profiles of temperatures on three areas (A, B, and C) are shown in Supplementary Fig. 13i.

For estimating temperature T under UV pulse irradiation, time to substitute in equations (6.2) and (6.3) was returned according to equations (6.8) and (6.9), respectively, every time UV on/off is switched (at each half time of period: 1.282 ms):

$$t_{UV\ on} = -\tau_{UV\ on} \ln\left(1 - \frac{T - T_0}{A}\right) \tag{6.8}$$

$$t_{UV\ off} = -\tau_{UV\ off} \ln\frac{T - T_0}{T_{max} - T_0} \tag{6.9}$$

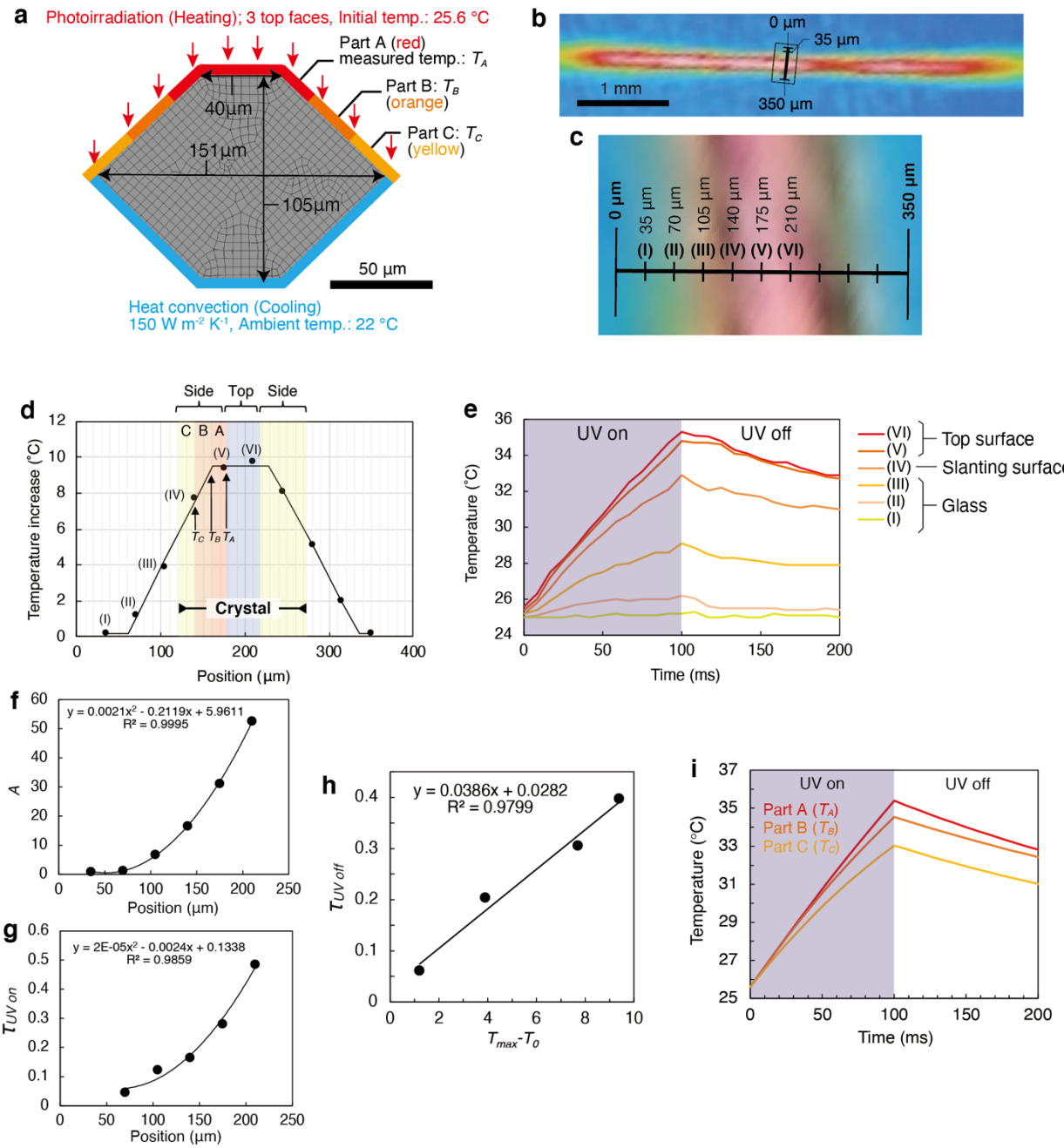

Supplementary Fig. 13 Relationship between position along the width direction and temperature change. **a** Geometry of the cross-section surface with temperature input areas of A, B, and C. Arrows of T_A, T_B, and T_C show temperature determination points of areas A, B, and C, respectively. **b** Temperature distribution of the crystal and the ambient air upon UV irradiation for 100 ms. Black line is coincident with the temperature measurement line along the width direction. Inset numbers indicate the position in accordance with the horizontal axis of **d. c** Enlarged view of the square in **b**. **d** Position dependence of the temperature increase upon UV irradiation for 100 ms. Blue region indicates the top face (width: 40 μm), and the red, orange, and yellow regions are the side area of A, B, and C, respectively. Arrows of T_A, T_B, and T_C indicate temperature determination points of areas A, B, and C, respectively. Inset symbols indicate the temperature measurement points which correspond to the legend of **c**. **e** Time dependence of temperatures of six points I–VI. **f, g** Position dependence of the maximum temperature increase A (**f**) and the time constant $\tau_{UV\,on}$ (**g**) upon UV irradiation. **h** Position dependence of the time constant $\tau_{UV\,off}$ after stopping UV irradiation. **i** Time dependence of temperature changes on part A, B, and C (T_A, T_B, and T_C, respectively).

6.2. Simulation II of bending of crystal III based on the irradiated light energy

For the simulation II, the photothermally generated heat was considered to be coincident with the irradiated light intensity, and the heat flux was applied to the top and two upper slanting faces as the photothermally generated heat, summarized in Supplementary Fig. 14a. The UV light was irradiated straight to the top surface of the crystal, so the heat flux to the top face was set to be the same value as the irradiated light intensity (14,560 W m^{-2}). Unlike the top face, UV light irradiated to two upper slanting surface from the direction of the incident angle (43.67°), thus the heat flux to those surfaces was set to be (14,560 W m^{-2} × cos 43.67° =) 10,532 W m^{-2}. The heat convection was considered to be occurred on three bottom surfaces for fitting.

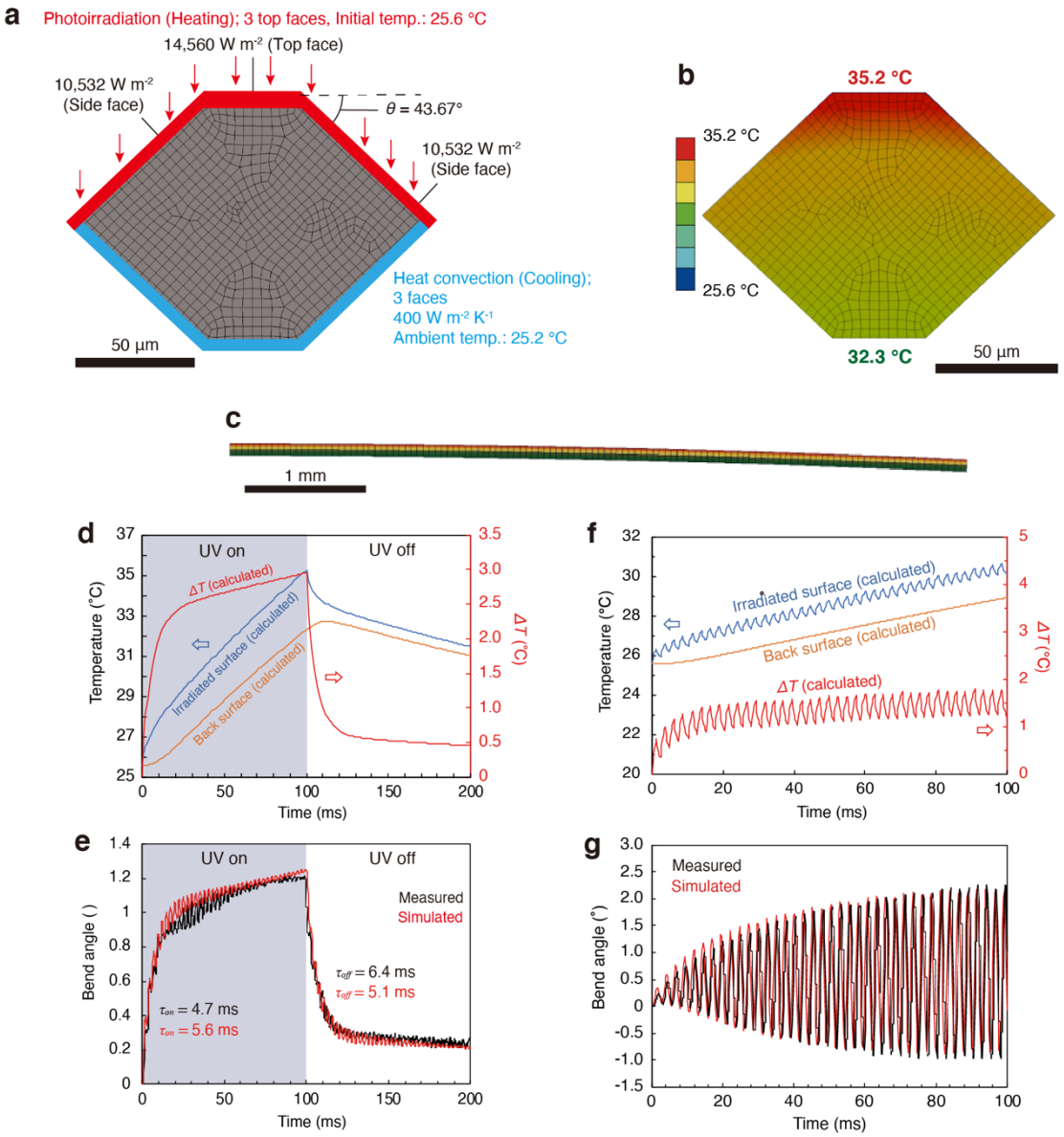

Supplementary Fig. 14 Simulation II of **1β** crystal III bending by the photothermal effect and the natural vibration, based on the irradiation light intensity. **a** Meshing and heat condition for non-steady heat conduction analysis on simulation Ⅱ. **b, c** Simulated temperature distribution after UV laser irradiation for 100 ms: the (100) cross-section (**b**) and the side view of bent crystal (**b**). **d, e** Bending simulation with and without UV irradiation for 100 ms: time dependence of top surface (blue, measured), back surface (orange, calculated) temperature and temperature difference between two surfaces (ΔT, red, calculated) (**d**), time profiles of measured (black) and simulated (red). The inset values of τ_{on} and τ_{off} indicate the time constants for bending and straightening (**e**). **f, g** Simulation of amplified bending under 390 Hz pulse UV irradiation: time dependence of top surface (blue, measured), back surface (orange, calculated) temperature, and the temperature difference between two surfaces (ΔT, red) (**f**), time profiles of measured (black) and simulated (red), amplified bend angles (**g**).

7. List of movies

Supplementary Movie 1: Non-resonated natural vibration associated with large photothermally driven bending of **1β** crystal III upon UV laser (375 nm, 1456 mW cm^{-2}) irradiation for 100 ms and then turning off the UV light, and simultaneous monitor of surface temperature with an IR thermography camera (realtime → slow motion × 0.01) (MP4).

Supplementary Movie 2: Resonated natural vibration of **1β** crystal III upon 390 Hz pulsed (1.282 ms on, 1.282 ms off) UV laser (375 nm, 1,456 mW cm^{-2}) irradiation (slow motion × 0.02) (MP4).

Supplementary Movie 3: Bending simulation I of **1β** crystal III based on measured surface temperature; 390 Hz non-resonated natural vibration with large photothermally driven bending upon UV laser irradiation for 100 ms and then turning off the UV light (slow motion × 0.02) (MP4).

Supplementary Movie 4: Bending simulation I of **1β** crystal III based on measured surface temperature; 390 Hz resonated natural vibration upon 390 Hz pulsed (1.282 ms on, 1.282 ms off) UV laser (375 nm, 1,456 mW cm^{-2}) irradiation (slow motion × 0.02) (MP4).

Supplementary Movie 5: Bending simulation II of **1β** crystal III based on irradiated light energy; 390 Hz non-resonated natural vibration with large photothermally driven bending upon UV laser irradiation for 100 ms and then turning off the UV light (slow motion × 0.02) (MP4).

Supplementary Movie 6: Bending simulation II of **1β** crystal III based on irradiated light energy; 390 Hz resonated natural vibration upon 390 Hz pulsed (1.282 ms on, 1.282 ms off) UV laser (375 nm, 1,456 mW cm^{-2}) irradiation (slow motion × 0.02) (MP4).

8. Supplementary references

S1. Cliffe, M. J. & Goodwin, A. L. *PASCal*: a principal axis strain calculator for thermal expansion and compressibility determination, *J. Appl. Cryst.* **45**, 1321–1329 (2012).

S2. Morikawa, J., Hashimoto, T., Kishi, A., Shinoda, Y., Ema, K. & Takezoe, H. Critical anomalies in thermal diffusivity of liquid- crystalline terephthal-bis-(4-n-butylaniline). *Phys. Rev. E: Stat., Nonlinear, Soft Matter Phys.* **87**, 022501 (2013).

S3. Ryu, M., Batsale, J. C. & Morikawa, J. Quadrupole modelling of dual lock-in method for the simultaneous measurements of thermal diffusivity and thermal effusivity. *Int. J. Heat Mass Transfer* **162**, 120337 (2020).

S4. Ryu, M., Takamizawa, S. & Morikawa, J. Thermal diffusivity of organosuperelastic soft crystals during stress-induced phase transition. *Appl. Phys. Lett.* **119**, 251902 (2021).

S5. Hasebe, S., Hagiwara, Y., Komiya, J., Ryu, M., Fujisawa, H., Morikawa, J., Katayama. T., Yamanaka, D., Furube, A., Sato, H., Asahi, T. & Koshima, H. Photothermally Driven High-Speed Crystal Actuation and Its Simulation, *J. Am. Chem. Soc.* **143**, 8866–8877 (2021).

S6. Hasebe, S., Hagiwara, Y., Takechi, K., Katayama, T., Furube, A., Asahi, T. & Koshima, H. Polymorph-Derived Diversification of Crystal Actuation by Photoisomerization and the Photothermal Effect. *Chem. Mater.* **34**, 1315–1324 (2022).

S7. Hasebe, S., Hagiwara, Y., Hirata, K., Asahi, T. & Koshima, H. Crystal Actuation Switching by Crystal Thickness and Light Wavelength. *Mater. Adv.* DOI: 10.1039/d2ma00825d. (2022).

S8. ANSYS® Academic Research Mechanical, 2021 R1 (ANSYS Inc., Cannonsburg, USA, PA, 2021).